# Design, aerodynamics, and vision-based control of the DelFly

**G.C.H.E. de Croon, K.M.E. de Clercq, R. Ruijsink, B. Remes, and C. de Wagter**

Aerospace Software and Technologies Institute, Technical University of Delft

Rotterdamseweg 380, 2629 HG, Delft, the Netherlands

## ABSTRACT

Light-weight, autonomous ornithopters form a promise to observe places that are too small or too dangerous for humans to enter. In this article, we discuss the DelFly project, in which we follow a top-down approach to ever smaller and more autonomous ornithopters. Top-down signifies that the project always focuses on complete flying systems equipped with camera. We give arguments for the approach by explaining which findings on the DelFly I and DelFly II recently led to the development of the DelFly Micro: a 3.07-gram ornithopter carrying a camera and transmitter onboard. These findings concern the design, aerodynamics, and vision-based control of the DelFly. In addition, we identify main obstacles on the road to fly-sized ornithopters.

## 1. INTRODUCTION

One of the goals of research on Micro Air Vehicles (MAVs) is to arrive at fly-sized MAVs that can fly autonomously in complex environments. Such MAVs form a promise for observation tasks in places that are too small or too dangerous for humans to enter. Their small size would allow the MAVs to enter and navigate in narrow spaces, while autonomous flight would allow the MAV to operate at a large distance from its user.

The requirements for the MAV described above are legion. For one, it needs to be as light as possible for endurance, while having enough onboard sensors and processing that allow it to navigate autonomously. Moreover, it needs to be able to hover, allowing it to get a "good look" at the object of observation. At the same time, it needs to fly at higher speeds to travel larger distances.

It may come as no surprise that in their quest for a fly-sized MAV, researchers draw inspiration from natural systems. For example, flying insects comply with the requirements mentioned above and can thus provide inspiration for solving the engineering problems encountered in the creation of a fly-sized MAV. One of the key properties of systems inspired by flying insects is that they use flapping wing propulsion (they are *ornithopters*)[1,2,3,4,5,6,7,8,9]. Especially at smaller sizes, this propulsion method produces more lift than fixed wing configurations[10,11,12,13].

Essentially, there are two main approaches to creating small autonomous ornithopters: *bottom-up* and *top-down*. In the bottom-up approach, one starts by creating all the tiny parts that are deemed important to a fly-sized ornithopter[2,14,15]. The most remarkable example of this approach is the work of the Harvard Microrobotics Laboratory. They succeeded in creating a 60 mg robotic insect, which can produce sufficient lift to take off vertically. To achieve this, they made use of Smart Composite Microstructures (SCM)[2]. The robotic insect was still fixed to taut guide wires that restricted the robot to vertical motion and provided both energy and control. In future work, the group plans to allow all degrees of freedom and to incorporate onboard energy supply, sensors, and processing.

In the top-down approach, one starts with a fully functioning (relatively large-scale) ornithopter. By studying this ornithopter, theoretical insights can be gained into the complex of necessary properties for a smaller version. Research then progresses by creating and studying ever smaller systems, while always maintaining a fully functioning flying robot. One advantage of this approach is that it allows interplay between theory and practice. Especially in the field of artificial intelligence, having a physical and fully functioning robot is of great value[16,17,18]: real-world tests force the experimenters to take into account all aspects of the robotic system. In addition, they reveal physical properties of the system that

can be exploited by the algorithms.

In this article, we focus on the top-down approach followed in our *DelFly* project[19]. We give arguments for our approach, and explain how findings on the (larger) DelFly I and DelFly II led to the creation of the DelFly Micro, a 3.07-gram ornithopter carrying a camera and transmitter onboard (see Figure 1). Carrying a camera is essential, since the project focuses on vision controlled ornithopters.

In the article we discuss the most important aspects of the DelFly ornithopters in turn. First, we give insight into the design choices of the DelFly (Section 2). Then, we study the aerodynamics of the DelFly, and explain how the results may improve its design (Section 3). Subsequently, we discuss the electronics on the DelFly, and the corresponding problems that we had to solve (Section 4). We report on our approach to reaching autonomous flight in (Section 5). Finally, we discuss the DelFly Micro and identify the main challenges ahead to developing even smaller versions (Section 6).
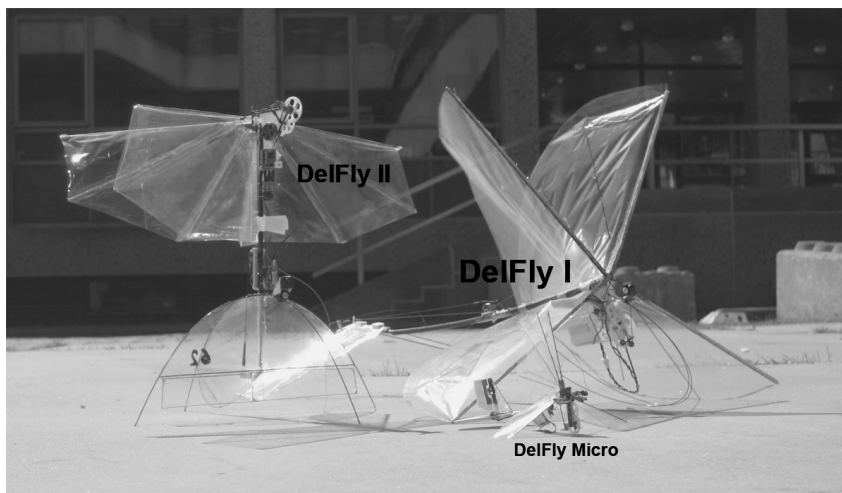


**Figure 1.** DelFly I (50 cm span, 21.00g), DelFly II (28 cm span, 16.07g) and DelFly Micro (10 cm span, 3.07g).

## 2. DESIGN AND MATERIALS

In this section, we first motivate the general concept of the DelFly design: a biplane wing model (Subsection 2.1). Subsequently, we discuss the crank mechanism (Subsection 2.2), the wings (Subsection 2.3), the tail (Subsection 2.4), and the fuselage (Subsection 2.5). For all these parts, we explain how and why they have evolved over time, as a result of measurements and flight experiences.

### 2.1 General Concept.

The main aim of the DelFly design was to achieve an airborne camera platform with good flight characteristics. This ruled out drastic design revolutions compared to existing ornithopter designs. For example, (semi-) rigid wings articulated with many degrees of freedom were not considered. Such a system is difficult to control, since there is a lack of knowledge both on how its movements should and could be actuated in a sensible manner.

Consequently, three existing ornithopter concepts were studied for the creation of the DelFly I[20]. The first concept was a simple monoplane with one set of wings. The second was a biplane concept where two sets of wings were placed above each other. These wings moved in counter phase on a common rotational axle. The third concept involved a tandem configuration, where two wings were placed one behind the other. The wings of this concept also moved in counter phase. We wanted to test the three concepts with respect to the flight speed, the power consumption, and the stability of the ornithopter's body during flight. This last characteristic is vital for the ornithopter's role as a camera platform.

To test the concepts, models were made of simple balsa wood and commonly available tissue. The models were powered by rubber bands. The models are well known in the indoor free flight model world and were acquired as standard kits[21]. All three models had the same span, chords, and weight. As a consequence, the wing loading of the monoplane was two times as high as the others. Each model was flight tested, while measuring the flying distance, the flight time, and the number of winds of the rubber band before and after the flight. The latter two quantities can be used to calculate the flapping

frequency and the energy stored in the rubber band before and after the flight. Table 1 shows the average flight speed, power consumption, and rocking amplitude (periodic fuselage motion perpendicular to the flight path) for the three models.

Table 1: Test results on model planes used to define the DelFly concept [20].

|  | **Monoplane** | **Biplane** | **Tandem** |
|---|---|---|---|
| Average flight speed | 2.35 m/s | 1.40 m/s | 1.36 m/s |
| Power consumption | 0.75 W | 0.69 W | 1.00 W |
| Rocking amplitude | ~80 mm | ~0 mm | ~0 mm |

The table shows that the monoplane had the highest flight speed: a logical result of the high wing loading., For the given weight and size it consumed more power than the biplane model. Further analysis indicated that a monoplane with the same total wing area as the biplane would consume less power. Yet, this would increase the size of the MAV, contrasting the emphasis on small MAV-dimensions. The lower power consumption for the same size led us to select the biplane model. An additional advantage of the biplane model is that the low rocking amplitude of the fuselage in flight makes it a suitable camera platform.

## 2.2 Crank mechanism.

DelFly I had a crank mechanism as the main wing axle, shown in the left part of Figure 2. Its gear axles were placed in the flying direction. The advantage of this setup was that it yielded simple connecting rods with all movements in one plane. The disadvantage was that the phase between the two sets of wings was not equal, which led to a rotational reaction movement on the fuselage and thus the camera. This resulted in blurred camera images.

To overcome this lack of symmetry, we designed a new drive mechanism with the gear axle perpendicular to the flying direction. This setup is shown in the right part of Figure 2. Used on the DelFly II, this mechanism has proven to give a good symmetrical movement with no rocking motion of the fuselage. The highest thrust (force along fuselage axis) is required during hover. It was achieved by maximizing the flapping amplitude (flap angle) and forced us to attach the connecting rod as close to the fuselage as possible.
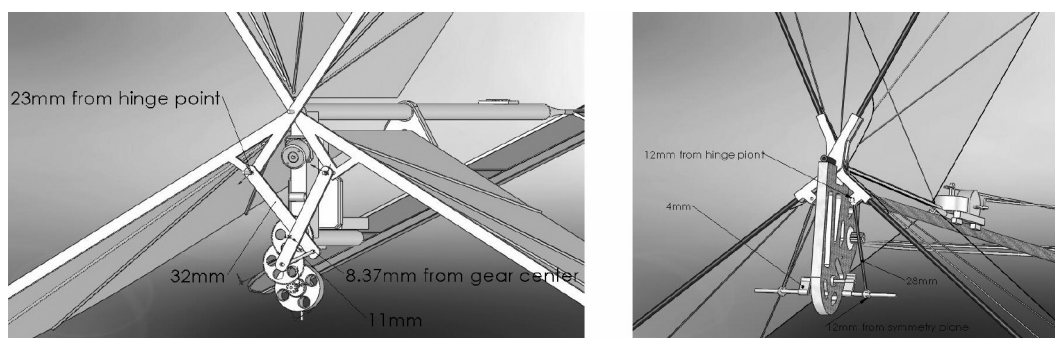


**Figure 2.** Schematics of the crank mechanism of DelFly I (left) [20] and DelFly II (right).

## 2.3 Wings

The design of the wings started with the standard model kits, a form that has been known for decades. The material consisted of 6 microns Mylar foil. A stroboscope box was constructed to visualize the

form of these wings during motion[20]. The time lapse study indicated that the flexibility of such wings was too high. Inspection of the wing deformations showed that the trailing edge of the wing was completely folding while flapping. As such, it did not contribute efficiently to the generation of lift. Therefore, we introduced stiffeners into the wing of the DelFly I. Several concepts were tested and two stiffeners gave the best result.

After flying for an extended time with the DelFly I, the foil deteriorated and a higher flapping frequency was needed for hovering. In addition, the parts of the wing surpassing the straight lines in between the stiffeners would curl up. This was an indication that these wing parts were still spurious, and they disappeared in the design of both the DelFly II (Figure 3) and DelFly Micro.

The shape of the wing is an important determining factor for the lift. Therefore, thorough studies on the relation between wing shape and lift may contribute significantly to further minimization of ornithopters[1,11]. An example of such a study is [11]. Interestingly, the shape of the DelFly wings is very similar to their wing type 'A', which produces a high lift at 0 wind velocity. Our own wing setup was more thoroughly tested in later phases with high speed camera visualization[22], and recently with Particle Image Velocimetry (PIV) as described in Section 3.

## 2.4 Tail

The DelFly I had a V-tail, because of its mechanical simplicity. An inverted V-tail was used in order to give a favorable yaw-roll coupling, making the turns without ailerons smoother.
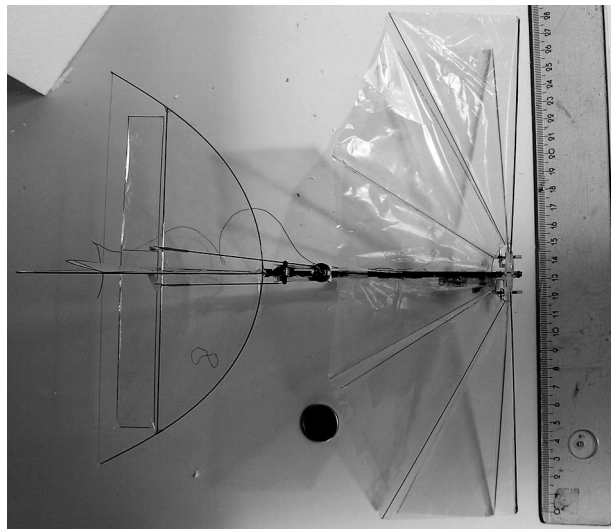


**Figure 3.** Top view of the DelFly II with two stiffeners per half wing.

During the DelFly II development the inverse V-tail was abandoned for a conventional cross-tail. The reason behind that is the placement of the tail in the wake of the flapping wings during hover. With the original inverse V-tail the control of the longitudinal motion became rather marginal in this situation.

In addition, the tail was placed closer to the wings. This improved the stability and control during the hover without reducing these aspects during cruise. The interaction of the horizontal tail with the vortices shedding from the wing might be playing a part, but this has not yet been studied.

The tail of some versions of the DelFly II is extended, such that the vehicle can take off and land as a tail sitter. During the testing of the concept a flight has been performed with 39 take-off and landings on a single battery charge, see [19].

## 2.5 Fuselage.

The rear part of the fuselage is a light carbon tube. As all commercial tubes were found to be too heavy, a tube was constructed in-house. Basically it consists of a carbon sleeve that is impregnated with epoxy. When the nominal diameter of the woven carbon sleeve is small, the fibre orientation is strongly tangential which yields high torsion stability. When the nominal diameter is large, the orientation is more longitudinal giving more bending stability. The latter is used on the fuselage.
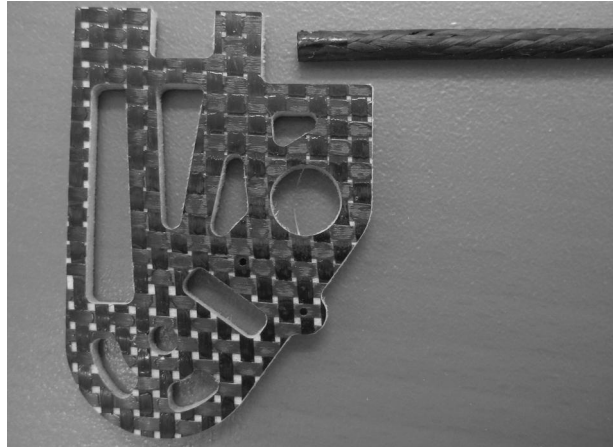
**Figure 4.** The fuselage front part and the rear end tube.

The front part of the fuselage is a sandwich construction. We have experimented with several methods to produce these. The current state of the art for DelFly II is a sandwich of 2.5 mm light balsawood between two single layers of 80 gr/m2 carbon cloth. A bigger sheet is impregnated under vacuum, then CNC milled to the right shape to ensure a good fit of the motor, gears and wing hinge (see Figure 4).

## 3. AERODYNAMICS

Insect flight has been a source of inspiration during the development of DelFly. Flapping wings, as used by birds and insects, simultaneously generate lift and propulsion and subsequently introduce a favorable maneuverability and wide flight envelope. A fully controllable vehicle can be achieved with a relatively simple drive mechanism which offers the potential of miniaturization.

Although insects with two pairs of wings mostly disappeared through evolution, DelFly is equipped with this wing configuration. The choices made for DelFly's particular wing configuration are clarified in Subsection 3.1. In order to further decrease the overall size of DelFly, preserving the excellent flight performance, a thorough understanding of the aerodynamics is necessary. Therefore, we give a theoretical description of the kinematics in Subsection 3.2. In Subsection 3.3, a theoretical flow analysis is applied to the typical wing motion and illustrated by observations on insects. The accordance of the theoretical to the actual flow field has been examined in an experimental campaign, as will be discussed in section 3.4.

## 3.1 The wing configuration

One of the most determining features of the DelFly's appearance is its wing configuration. The choice for this particular configuration is based on overall system requirements. It largely influences the aerodynamics and is crucial for the flight performance. As explained in Section 2, DelFly has been designed with two pairs of wings flapping in anti phase with the aim to create a stable camera platform. To maximize the lifting surface within the stringent size limitations, both wings are positioned on top of each other (left part of Figure 5). In order to obtain lateral stability in forward flight, the wings are positioned symmetrically with respect to the fuselage plane at a dihedral angle. A small clearance is provided between the upper and lower wing in their neutral position for preventing impact damage.

The wings move to and fro in a single plane. This motion will be termed the *translational motion*. Under combined inertial and aerodynamic loading, the wings rotate between subsequent strokes such that the anatomical leading edge always leads. We will call this the *rotational motion*. The upper and lower wings flap at the same frequency and over an equal flap angle. For the DelFly II the optimal flap angle and frequency for hovering, maximizing thrust (aerodynamic force along fuselage) for minimal power consumption has been determined experimentally [22]. It was found to be in between 30° and 36°. To maximize the payload capacity, the flap angle is maximized within the limitations of the drive mechanism. Due to inertia and elasticity the wings are dynamically twisted.
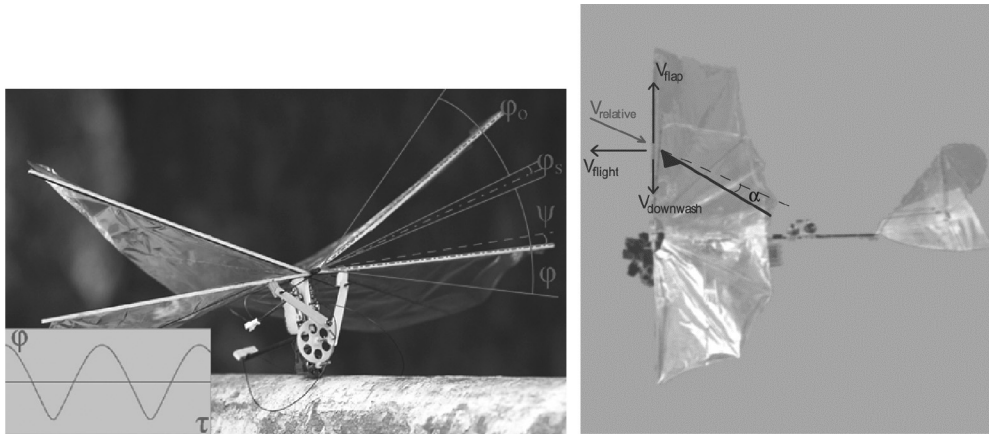
**Figure 5.** Left: Biplane wing configuration of DelFly. Indicated are the flap angle φ, the dihedral angle ψ and the clearance angle $φ_s$ Right: Schematic representation of the fluid velocity with respect to the wing section (side view of the DelFly in forward flight). The morphological lower surface is indicated by the triangle at the leading edge of the outlined wing section.

## 3.2 The flight kinematics

DelFly II attains an exceptionally broad flight envelope with the same configuration. Different throttle and elevator commands result in entirely different flight behaviours. The DelFly is not only capable to fly with a maximum forward speed of 7 m/s and to hover; it can even fly backwards with a speed up to 1 m/s[i]. An analysis of the typical wing motion and the aerodynamic forces explains how such a broad flight envelope is possible.

The velocity of the wing with respect to the air (right part of Figure 5), defined by the flight, flap and downwash velocity, is tangent to the wing path. Accordingly the lift and drag force are respectively perpendicular and tangent to the wing path. Figure 6 shows the wing path during fast forward flight, in which the forward velocity is bigger than the flapping velocity. The flap plane is positioned nearly vertically and the fuselage nearly horizontally, minimizing the drag. The tail is used as in a normal plane configuration.
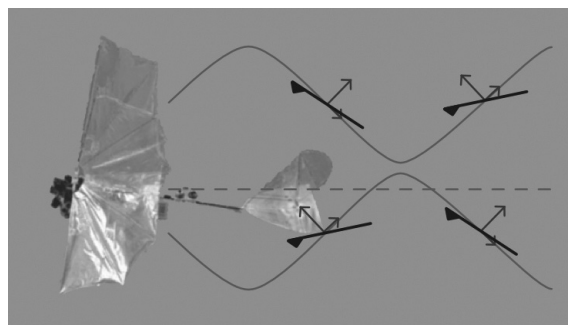


**Figure 6.** Schematic representation of the wing path for a DelFly in forward flight (solid lines). The morphological lower surface is indicated by the triangle at the leading edge of the outlined wing section. The resultant aerodynamic forces for both strokes are shown with arrows.

By pulling the elevator up, the body tilts nose-up and the flight speed decreases, until the flap plane becomes horizontal during hovering. The left part of Figure 7 shows the wing path and related forces for hovering flight. The effective velocity is now only defined by the flap and downwash velocity. The motion of the upper and lower wing pairs is symmetric, providing weight support but cancelling the

---

[1] Notably, when flying backwards with ~80% throttle and 100% elevator, the DelFly will turn around and can continue with a forward flight. This behavior may be useful in obstacle avoidance. If 100% throttle and 100% elevator is used, the DelFly will fly backwards and climb with ~1m/s.

horizontal aerodynamic force. In hovering flight, the direction of the fluid velocity with respect to the wing section and the aerodynamic forces are symmetric for the upper and the lower wing. The arrows associated with the top right and bottom left wing section show that the anatomical lower wing surface, indicated by the triangle, does not always act as the aerodynamic lower surface.
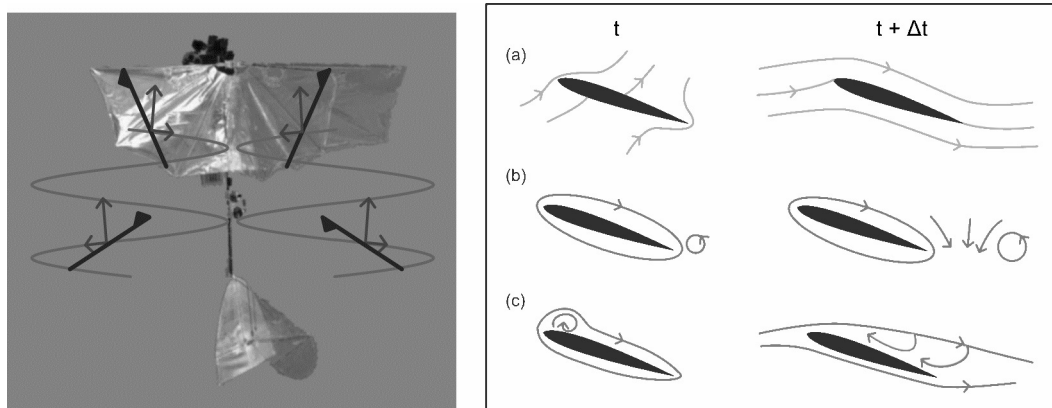


**Figure 7.** Left: Schematic representation of the wing path for a hovering DelFly. The morphological lower surface is indicated by the triangle at the leading edge of the outlined wing section. The resultant aerodynamic forces for both strokes are shown with arrows. Right: Schematic representation of the streamlines over time due to (a) Kutta condition, (b) Kelvin's theorem, and (c) dynamic stall.

## 3.3 Unsteady aerodynamics

Compared to steady airfoils, flapping wings are able to generate high lift coefficients due to unsteady aerodynamics. The lift enhancement has been attributed to specific fluid structures that occur during the different phases of the flap cycle[23]. Below, the role of these effects will be theoretically discussed and illustrated by observations on animals. Distinction will be made between the translational and rotational motion.

### 3.3.1 Translational motion

After rotation the wing is impulsively started in the translational phase. Air swirls around the sharp trailing edge introducing a region of intense vorticity (a in the right part of Figure 7, time *t*). Kelvin's circulation theorem[xiii] states that the time rate of change of circulation around a closed curve consisting of the same fluid elements is zero (b in the right part of Figure 7). Therefore a vortex, equal in strength but opposite in direction, is generated around the airfoil. The high-vorticity region moves downstream of the trailing edge and tends to roll up into a concentrated starting vortex As long as vorticity is shed from the trailing edge, the starting vortex grows stronger and so does the bound vortex, until the Kutta condition[24] is satisfied (a in Figure 7, *t+Δt*). This gradual build-up of circulation is called the Wagner effect[25]. Since the strength of the bound vortex is directly proportional to the velocity difference over the airfoil section, the build-up of vorticity is a measure of the increase in lift force generated per unit span. Because the total distance travelled by the wings during a half stroke is small, the circulation growing in a manner similar to Wagner's theory will remain lower than the steady value. Generally, the required lift to support body weight in flapping flight is larger than the lift producible by the wings in steady-motion. A source of additional lift has to be found.

Since the wings are impulsively started at an angle of attack higher than the stall angle, the phenomenon called dynamic or delayed stall[12] is expected. The separation associated with stall becomes well-developed (c in Figure 7, *t+Δt*), if the wing travels several chord lengths. During the brief period between *t* and *t+Δt*, the circulation, and thus the lift, exceeds the maximum quasi-steady stalled value. The circulation starts to grow at the beginning of the translational stroke and is proportional to the product of the chord and the span wise location[32]. The steady-state stall will not be reached if the stroke length covers only a few chords, as is the case for flapping wings.

When the translational wing motion stops at the end of the stroke, no lift or circulation should be left. The bound vortex swirls off the trailing edge, shedding as a stopping vortex (Figure 8). In the same

way as circulation grows at the beginning of a half stroke due to the Wagner effect, it decays gradually at the end. The decaying vorticity will interfere with the build up of circulation on the following half stroke, which is in the opposite direction. Because of the absence of flight velocity in hovering flight, the shed vorticity moves slowly down into the wake. The stopping vortex of one stroke is in the same sense as the starting vortex of the next. These vortices may shed together, hampering the formation of the new stroke's bound vortex. This reduces the lift.
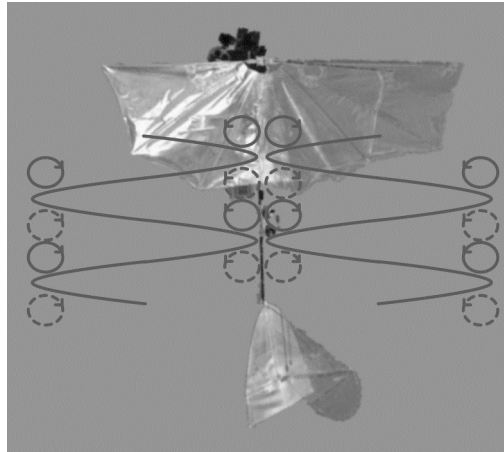


**Figure 8.** Schematic representation of the starting (solid) and stopping (dashed) vortex sequence.

At the wing tips, the flow is forced from the high-pressure region underneath the foil to the low-pressure region on the top, forming the tip vortices. These tip vortices in combination with the starting and stopping vortices form a rectangular vortex ring.

How these mechanisms manifest in reality has been the topic of experimental studies on a broad range of species. Especially interesting in the scope of this study are the results of research on the hawk moth Manduca Sexta, which operates in a Reynolds range corresponding to the DelFly II. Similarly to DelFly, the hawk moth tilts his flap plane horizontally to hover. The studies by Ellington's group[26,27] confirmed the existence of a leading edge vortex formed above the wing during down stroke. The dynamic stall mechanism is clearly responsible for the leading edge vortex generation, since the circulation builds up during the translational stroke. The vortex increases with time in both size and strength along the wingspan, proportional to the product of the chord length and the span wise location. This implies that the vortex grows as a conical spiral and that no vortical structure is present between the wing bases.

### 3.3.2 Rotational motion
At the end of the translational stroke, the wings decelerate and rotate in preparation for the subsequent half-stroke. During rotation near the neutral position both wings come together. In contrast, the rotation at the other end of the wing beat is an isolated rotation.

The first reasons to choose for wing surfaces constructed of Mylar foil with carbon stiffeners were its light weight and strong shear resistance. However, its flexibility introduces some interesting aerodynamic features. The wings profile changes continuously during a wing beat sequence under influence of both inertial and, to a large extent, aerodynamic loading[1]. The wing flexibility is especially decisive during rotation. The changes in wing attitude during a flap cycle have been determined by visual inspection of high speed camera images of a hovering DelFly II[22].

As the wings decelerate near maximal flap angle, the angles of attack increase until the wing is perpendicular to the stroke (Figure 9a-b). Near the middle of rotation (Figure 9c-d) the wing flexes: the leading edge accelerates to the opposite direction, forcing the upper part of the wing to rotate, while the trailing edge stays almost stationary. Due to this flex mechanism[25], the leading edge has a greater velocity and vorticity may shed into a separation vortex at the leading edge instead of the conventional starting vortex shed from the trailing edge. This leading edge vortex is of the correct sense for the following half-stroke and stays attached to the wing at the beginning of translation. The leading edge accelerates at the beginning of the next half stroke and the wing unflexes (Figure 9e). The bound

vorticity is likely to roll up around the stationary trailing edge and shed as a combined starting and stopping vortex when the wing unflexes. This mechanism would provide the wing with a net circulation at the beginning of the following half stroke, which skips the gradual increase of lift.
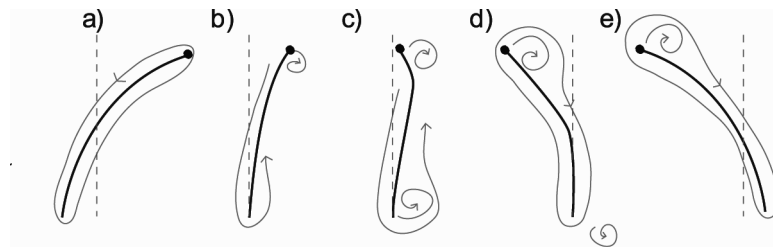


**Figure 9.** Schematic representation of the flex mechanism. The dot on the outlined wing section is indicating the location of the leading edge. The arrows represent the streamlines. The dashed line is at a fixed position in space.

Smoke visualization with tethered Manduca Sexta moths[26] investigated the use of the flex mechanism at the end of the down stroke. At the moment that the leading edge starts to rotate, the fore- and hind-wings flex. The increase in the velocity at the leading edge induces vortex shedding at the anatomic lower surface. This new leading edge vortex is in the correct sense as to enhance the bound circulation during the subsequent stroke. However, it does not remain attached to the wing.

Near minimal flap angle, the angles of attack increase as the wings decelerate and the upper and lower wings touch along their surfaces. First the leading edges approach, the wings curve along their camber and the meeting point smoothly moves along the wing surfaces towards the trailing edges, as sketched in Figure 10a-d. By expelling air downwards, this clap mechanism[28] may produce a momentum jet augmenting lift. Otherwise the lift enhancement could be interpreted as a method to extend lift generation till the clap is completed. Since both wings' bound vorticity is equal in strength but opposite in sign, Kelvin's theorem applies without the need for a stopping vortex to be shed.
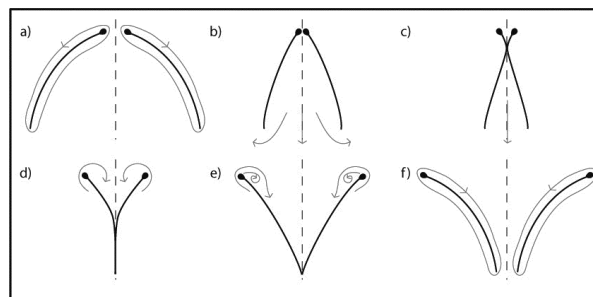


**Figure 10.** Schematic representation of the clap and peel mechanism. The dot on the outlined wing section is indicating the location of the leading edge. The arrows represent the streamlines. The dashed line represents the neutral position of the wings.

Already before the clap has been completed, the leading edges start separating again, the wings curve towards the opposite side and the surfaces peel apart, as can be seen in Figure 10e-f. Due to this peel, fluid flows over the wing surfaces into the opening gap creating a circulation in opposite direction around both wing[28]. The circulation is expected to grow linearly with the distance from leading edge to separation point[25]. No starting vortices would be shed, since the bound vortex of one wing acts as the starting vortex of the other one. As the wings separate and move apart in the next stroke, enhanced lift would immediately be generated from the fling circulation, circumventing the gradual growth and decay of circulation by the Wagner effect.

Examples of insects using clap and fling as lift enhancement mechanism typically operate in a lower Reynolds range. On a dynamically scaled robotic model of a fruit fly, Lehmann[29] recently investigated lift enhancement due to the fling mechanism. The clap mechanism was found to attenuate lift force. On the same model, Poelma[30] demonstrated the existence of leading and trailing edge vortices.

## 3.4 Experimental results

Recently, we performed experiments on a full-scale and non-simplified model of DelFly II to verify the existence of lift enhancing vortex structures, as could be expected from the previous theoretical discussion. Here, we briefly discuss the main experiments and results. For a more extensive discussion of these experiments, we refer the reader to [31]. The data obtained in this study will be evaluated to contribute to the improvement of the aerodynamic characteristics of DelFly.

Since DelFly II differs from typical insects and birds in wing configuration, flapping frequency and wing size, only a restricted similarity in flow-field behavior is expected. The effects of complex wing kinematics, three-dimensional flow and fluid-structure interaction as a result of high wing flexibility are inseparably linked in the fluid dynamics behavior of DelFly II.

To simulate the hovering flight modus the wings were positioned vertically in a large cubic test volume where the surrounding flow was stationary. The mean wing beat frequency was selected as 13 Hz, which resembles a typical flapping frequency necessary to sustain hovering flight. The flow field around the wings was analyzed using stereoscopic Particle Image Velocimetry (PIV). Figure 11 shows the corresponding experimental setup. The measurement plane was oriented parallel to the chord at ¾ of the span and perpendicular to the dihedral line. Simultaneous force measurements indicate the contribution of visualized flow structures to the lift generation. The upward force was measured by miniature sensors Q70x5x9-H with a capacity of 20*g (g = 9.81 m/s$^2$).
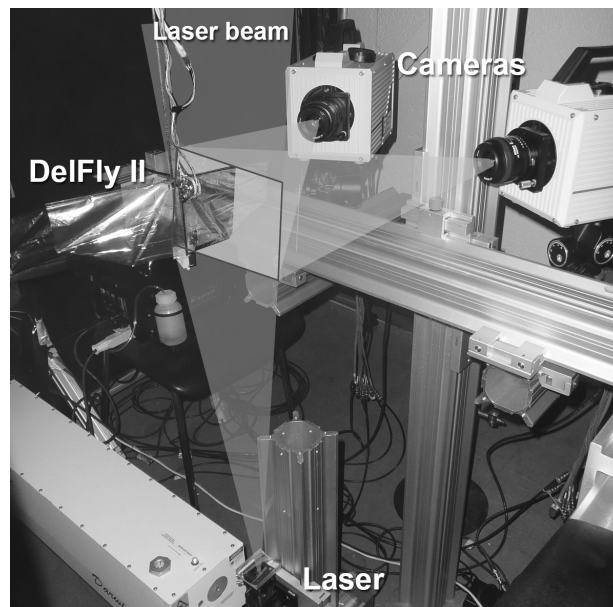


**Figure 11.** Photograph of the experimental arrangement: the laser beam illuminates a wing section of the DelFly II. The illuminated smoke particles are filmed by two cameras.

### 3.4.1 Heaving motion

We first visualized the trajectory of the imaged wing section, in order to investigate whether its trajectory resembles that of our theoretical discussion in Subsection 3.3.2. The trajectory, shown in Figure 12, indeed resembles the figures shown before. However, the leading edges do not move solely in the flap plane. This can be explained as follows. Preliminary tests on the DelFly II showed that it was not able to fly with round 0.7mm diameter carbon rods as leading edges. The rods were then cut in half, resulting in a D-shaped rod with the rounded surface facing forward. This modification did not only allow the DelFly II to fly forward, but also to hover. The essential difference with the circular rod is a lower stiffness in the direction perpendicular to the flap plane. Due to the fluid-structure interaction, the leading edges make a heaving motion in this direction (see Figure 12). During the acceleration in the beginning of the translational stroke, the wing foil pulls tight and the leading edge is pulled downwards. At the end of the stroke, tension is released and the leading edge moves back towards its original position. The wing tip trajectory with respect to the body is an elongated figure eight-shape.
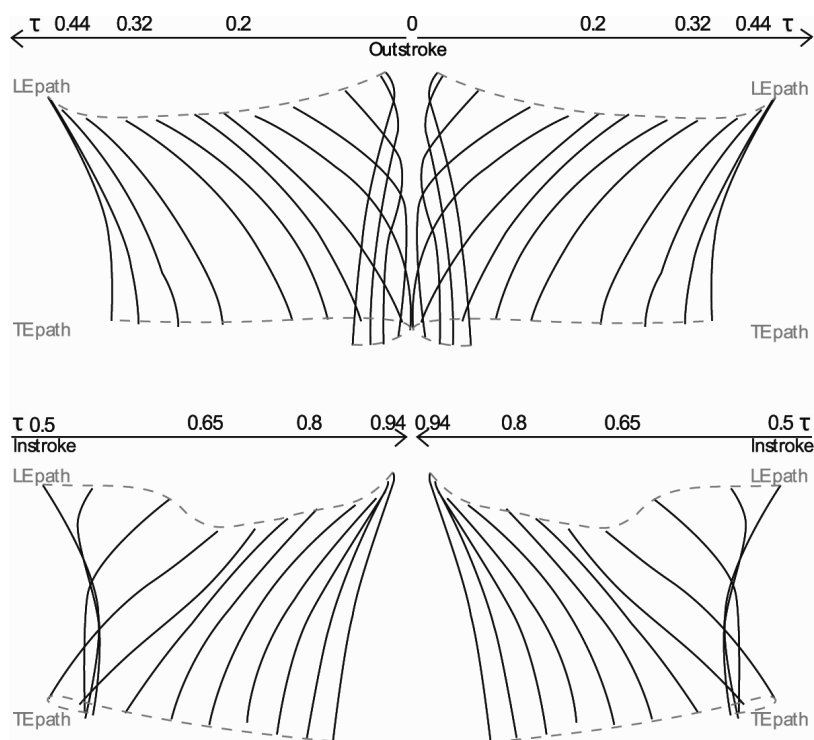
**Figure 12.** Schematic representation of the wing motion during one flap cycle. Instantaneous wing position and attitude is sketched with respect to the non-dimensional time. In- and outstroke are represented by upper and lower part respectively.

Similar wing paths have been observed for various insects[32]. Thanks to the upward motion during clap, the foil is pulled tight during the rotation. The downward leading edge motion during peel might reinforce the leading edge vortex generation by increasing the velocity of the fluid moving into the opening gap[33].

### 3.4.2 Flow field analysis

The results of the flow field analysis reveal that the most important augmentation in lift generation in the current test configuration of DelFly II is due to the inrush of air into the opening gap during the fling[31]. The occurrence of a leading edge vortex during fling cannot be assessed unambiguously from the PIV result because of the poor accuracy near the wings, but is doubtful since the inrush of air decreases the angle of attack considerably. Contrary to the expectation in our theoretical discussion, we did observe starting vortices at the end of the peel.

Another significant contribution to the lift generation might be the generation of a leading edge vortex at isolated wing rotation. The expected expelling jet during clap could not be observed. This is attributed to the high flexibility of the wing foil. More details on these results can be found in [31].

Based on the absence of an expelling jet during clap, it is suspected that a better aerodynamic performance of the DelFly could be attained by more rigid wing surfaces. This would increase the positive contribution of the clap mechanism to the lift generation without disturbing the favorable fling effect.

## 4. ELECTRONICS

There is no combination of off-the-shelf components that can be used for the electronics of ornithopters as small as the DelFly II and the DelFly Micro. In this section, we describe the various electronic components of the DelFly: the power source (Subsection 4.1), the motor (Subsection 4.2), the radio control system (Subsection 4.3), and the video system (Subsection 4.4). We explain how we improved some of the components over time for optimizing their performance on our flapping wing platform.

## 4.1 The Power Source

The power source to the ornithopter is an important design aspect. Its power- and energy density is crucial for the performance. As the absolute weight of the power source is very low many technologies that can be used in big scale are not feasible in the scale of a Micro Air Vehicle, let alone a Nano Air Vehicle (NAV). Fuel cells, nuclear generators, internal combustion engines, and many others are not (yet) applicable at this scale.

Disposable or rechargeable batteries have reached performance levels that allow successful flight scenarios. In the Delfly we use the easily available rechargeable Lithium Polymer batteries. The latest types of these batteries can deliver an energy density of 170 Wh/Kg and a power density of 4000 W/Kg sustained. The versions in the mass range of 1 to 4 gram, relevant for MAVs and NAVs are less efficient but still attain 130 Wh/Kg respectively 2600W/Kg. More modern battery concepts as the Lithium Sulphur type can almost double the energy density but they still do not match the required power density.

## 4.2 The Motor

When the power source is electric the drive motor is also electric. We first explain the drive mechanism on the DelFly. Then, we describe the consequences of this choice on our design of the motor.

### 4.2.1 Drive Mechanism

In an ornithopter we need an oscillating movement of the wings, with a frequency of between 8 and 50 Hz, depending on vehicle size and flight regime. One could employ actuators that directly produce a linear movement with a suitable force. However, this leads to the following problem. In almost all electric to mechanic conversion, the size and mass of the system are proportional to the force. Therefore, the power should be proportional to the force times the desired frequency. To reach a good power at low mass we need a high frequency at a low force. This cannot be achieved with conventional linear or reciprocating actuators.

Still the best solution yielding a favorable power density, we have found, is a high RPM electric motor with a gear set to match the rpm and the flapping frequency plus a crank mechanism.

### 4.2.2 Development of the Motor

The DelFly I featured a small coreless pager motor (MK07-2.3 red[34]). The problem of this motor was that it would in general provide only a few minutes of sustained flight, and usually wore out within an hour. The reason for this was the low efficiency of 35%, which led to overheating and expansion of the rotor inside the motor.

For the DelFly II we developed a brushless motor that matches the requirements in an ornithopter, in collaboration with the company DC Enterprises in India[35]. The resulting brushless motor was more efficient than the motor on the DelFly I, and delivered enough mechanical power to be able to hover (> 1.5 Watts or > 1kW / kg).



**Figure 13.** Image of a brushless motor.

A brushless motor (see Figure 13) can reach higher efficiencies and higher power densities than conventional brushed motors. In addition, there are no other wearing parts than the (ball) bearings. This makes the reliability of the motors several orders of magnitude better than their brushed brothers.

A brushless motor has a stator with 3 electric phases and an electronic controller produces a revolving electro-magnetic field. This makes the magnet rotor rotate. The timing of the controller can

be accomplished with magnetic sensors, which yields a well determined positional feedback of the rotor. These sensors can be avoided in more sophisticated controllers where the position of the rotor in relation to the stator phase is measured by means of the EMF voltage from the non-energized winding. The timing can be determined well when the motor runs smoothly with a constant or slowly changing rpm.

In the development of the DelFly motor and controller we have found that the determination of the timing is hampered by two aspects of uneven rotation.

1.    The first prototype of the motor did run very well with a propeller but would not run smoothly with the flywheel effect of only a small polyacetal pinion on the axle. This is the uneven running within one rotation of the motor.

2.    The first problem resolved there was the uneven load during one flapping cycle. Near the point where the flapping direction changes, the load on the motor changes abruptly also leading to timing difficulties.

The first problem was that the cogging torque of the motor produces a very swift speed change within each cycle of the rotation. At high rpm the timing was adequate, but the motor would not run at medium and low speeds necessary for our drive mechanism. In collaboration with Dr. E. Lomonova of the Eindhoven University we have made a magnetic simulation of the motor to find ways of reducing the cogging torque. With the help of simulations, we studied whether it was possible to reduce the cogging torque by varying the magnetic structure of the motor, the number of magnets, and the magnetic *embracement*: the percentage covered by magnets over the circumference of the rotor.

The original motor had 3 x 3 = 9 stator phases and 12 magnetic poles and a magnetic embracement of 100%. The embracement can be varied gradually by changing the sizes of the magnets in the motor. The left part of Figure 14 shows the relation between the embracement (in %, x-axis) and the efficiency (in %, left y-axis) and cogging torque (in *N\*mm*, right y-axis). The simulation showed that reducing the embracement would also reduce the cogging torque. A minimum cogging torque was realized with an embracement of 64%. It decreased significantly, from 330 Nmm to 17 Nmm. However, the efficiency of the motor would also decrease from 59% to 52%, which was not what we were looking for.

Another option to reduce cogging torque was to change the magnetic structure of the brushless motor. Brushless motors can be made with a vast range of phase-pole combinations, some excellent, some marginal. The 9 phase-12 pole and 12 phase-14 pole approach are the most common but others can behave well. A 9 phase-10 pole version was simulated and found to be very suitable.

The simulations showed that an embracement of 83% would lead to almost zero cogging torque with an efficiency as high as the original motor. This could be achieved with 10 of the original 12 magnets spaced evenly around the circumference of the rotor, with an embracement of ~83%. Without new tooling, an extremely low cogging torque was promised with an equally high efficiency as the base version (while maintaining the same rpm of the electromagnetic field). Due to the reduced number of magnets the actual mechanical rpm was 20% higher (see the right part of Figure 14). This formed no problem, as a two stage gearing was needed anyway and only the ratio had to change. In addition, the winding scheme for a 10 pole motor is different from the 12 pole version but that was easily implemented.
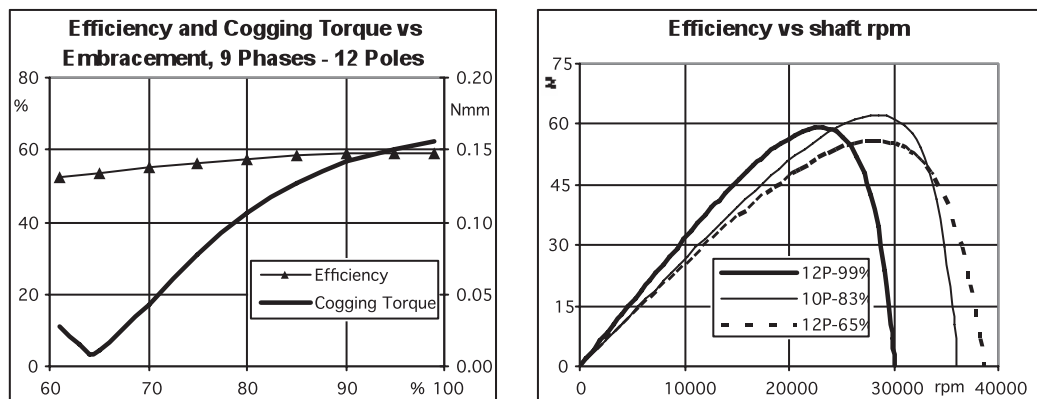


**Figure 14.** Left: Effect of the embracement on the efficiency and the cogging torque.   Right: Efficiency vs. shaft rpm for different brushless motor configurations

The second timing problem was caused by the uneven load during the flapping cycle of the ornithopter. The quick load changes are problematic for the commutation of the motor as it has to take place some 20° before zero crossing of the EMF signals. When the motor speeds up too quickly this may lead to 'misfiring'. To solve this problem, we cooperated with both Micro Plane Solutions of France and MicroInvent of Slovakia. The solution involved both the hardware and the software of the motor controller. The EMF voltages needed to be measured more accurately by the hardware, and the measurements needed to be filtered differently by the software. In particular, there was a larger emphasis on measurements with respect to the predictions. The resulting controller is shown in the left part of Figure 15.
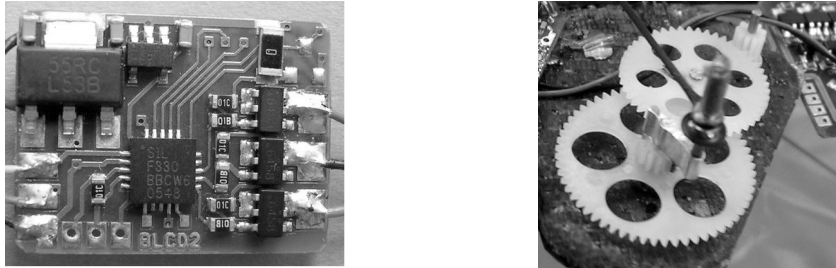


**Figure 15.** *Left*: Motor controller designed with Micro Plane Solutions of France and MicroInvent of Slovakia, in order to cope with the uneven load during one flapping cycle.
*Right*: The gears as used on the DelFly II.

To match the maximum required flapping frequency with the rpm range of the electric motor a gear ratio of 20:1 has been adopted. The gears are from polyacetal and have a module of 0.3. We have a 12 teeth pinion on the motor a 48/12 teeth idler gear. On the 60 teeth final gear a dual crank is fitted to actuate the two sets of wings (see right part of Figure 15). The motor we use is not the same as its commercial version, the Mighty Midget Nano[35].

## 4.3 The Radio Control System
A solid control of an MAV is equally important as a low weight. For the DelFly I, we have used the first version of a commercial 900 MHz system by Plantraco. This resulted in good control, but also in many small problems. These problems included: a way too low PWM frequency to power the then used brushed pager motor, no current limit on the actuator outputs made it not enough foolproof, awkward frequency control, and low quality transmitter sticks. Still, the system had as main advantage that it was very light.

Consequently, when designing the DelFly II, we searched for a different kind of system. When the MicroInvent Minor receivers came on the market we used them in conjunction with our standard 35 MHz transmitters. These receivers are very versatile and can be used with all kind of actuator and motor types.

Recently we are changing to a modified 2nd version Plantraco system. The Martin Newell "Rabbit" HipHop system, operates still on 868 or 900 MHz, but now with different soft and hardware. It is light to extremely light, and without all the problems we have encountered before. The system uses a frequency hopping algorithm to avoid any problem that could arise from frequency clashes, when flying in halls or during shows. The transmitter used is a HF module that couples to a decent transmitter front-end.

## 4.4 Actuators
The rudder and elevator of the DelFly are actuated by magnetic actuators (see Figure 16). At the beginning of the DelFly project these were the only systems of under one gram to provide adequate control. Conventional servos were available with a mass of around 2 grams at that time. Currently there are more options emerging, such as light-weight muscle-wire or Piezo actuators. Muscle-wire is a Shape Memory Alloy (SMA), which can become smaller by applying heat to it. Although it is in principle promising for light-weight actuation of ornithopters, its response time is currently too long for optimal control[36] and the efficiency is too low. Piezo actuators are more efficient, but still have too high voltage requirements for the batteries onboard the DelFly. The employed magnetic actuators offer just

enough control power, at a reasonably low weight and power consumption. They provide a smooth and fully proportional control. The actuators are the Plantraco MiniACT[37].
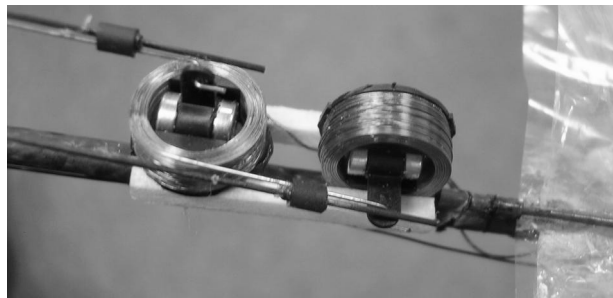


**Figure 16.** Magnetic actuators on the DelFly II.

## 4.5 The Video System

One of the principles of the DelFly is that it always is equipped with a camera system. The camera used has a dimension of 8 x 8 x 7 mm (see Figure 17). It is a special version of the MO-S588 ¼" CMOS NTSC camera with 380 lines and a 3.1 mm lens. This color version has a sensitivity of 1.5 Lux, while the EIA B&W version has a sensitivity of 0.05 Lux. The camera needs a clean power supply of 5 Volt at 40 mA. We developed an inductorless dc-dc converter that is mounted directly on the rear of the camera. The camera with dc-dc converter weighs exactly 1 gram. The transmitter works down to 3.3 Volt and can be driven directly from the flight battery.
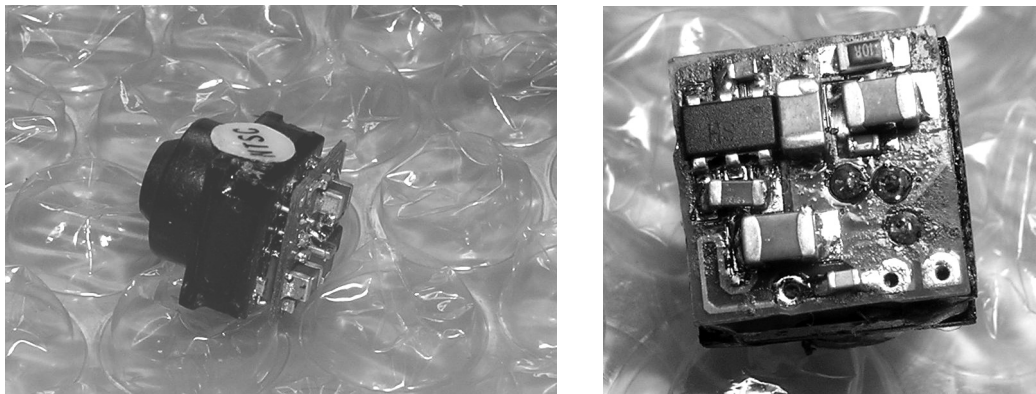


**Figure 17.** Two pictures of the DelFly II camera. Left: Side view of the camera. Right: Modified back-side of the camera

## 5. AUTONOMOUS FLIGHT

The DelFly II explained in the previous sections exhibits extremely stable flight for several minutes. The passive stable flight properties of the DelFly allow human pilots to control it without an extensive amount of training. The easy control and the acceptable quality of the platform's images allow experiments with autonomous flight.

In Subsection 5.1, we describe the challenges posed by autonomous vision-based flight and the various approaches followed in the literature to meet these challenges. Then, we describe our main autonomy experiments (Subsections 5.2 – 5.4).

## 5.1 Autonomous vision-based flight

Currently, many MAVs can perform autonomous outdoor flight. With an occasional exception[38], outdoor autonomous MAVs make extensive use of GPS (c.f. [39,40,41,42]). In indoor environments, GPS does not function properly, and autonomous flight becomes more difficult to reach. The vast robotics

literature cannot deliver ready-made solutions, since most autonomous robotic experiments have been performed with ground-based robots. Such robots face an inherently different problem than MAVs: taking no action will in general not cause harm to a ground-based robot, but will cause unpleasant encounters with walls, floor, or other obstacles for a flying MAV. In addition, ground-based robots can carry more and heavier sensors than MAVs. Infrared sensors and laser range finders are abundantly used in ground robotics (c.f. [43]). However, any sensor mounted on an MAV has to be traded off against other sensors.

All DelFlys have as sole sensor a video camera. The motivation for this choice is that a camera is a relatively light sensor for the amount of information that it can provide. In addition, camera images are easy to interpret for human observers. In the literature, there are three main approaches to reaching camera-based autonomous flight.

The first approach is to control an MAV with the help of external cameras (e.g., [44,45]). The images of the external cameras are used to detect different parts of the MAV. The exact position of these parts can be determined by triangulation methods and from these positions, the attitude of the MAV can be determined. With a measurement of the attitude of the MAV, it becomes possible to control even passively unstable MAVs such as helicopters. The first approach is the most successful, but also the most limited one: the MAV will only be able to fly in spaces in which there are (known) fixed cameras. Any exploration of unknown areas is thus impossible with this approach.

The second approach uses the onboard camera to accurately estimate the state of the MAV (3D position, pitch, yaw, and roll). Such a state estimate can be obtained by using a 3D model of the environment, which can either be prefabricated [46] or learned [47,48]. There is an increasing number of computer vision algorithms that succeed in building a model of the environment. However, they are currently still computationally expensive. Therefore, when entering a new room, the state estimation of the MAV does not work immediately. Remark that not all studies of this approach use an accurate 3D-model of the world to obtain an accurate estimate. Instead, some studies make specific assumptions on the space in which the MAV is flying. For example, state estimation can be performed with the help of `vanishing points' [49]. The vanishing points can be determined on the basis of parallel lines that are in sight. The method assumes that such lines are known and are in the field of view.

The third approach is a more bio-inspired approach to autonomous flight. Studies of this approach typically abandon a state estimate altogether and focus on training the right responses to incoming visual inputs. For example, in [50] optic flow is used in an onboard sensing and processing scheme to avoid walls on which special black-and-white textures were projected. The measured flow is directly coupled to the steering commands of the micro flyer. Studies of the third approach generally exploit optic flow (cf.[51,52,53]), and currently work best in textured environments. The reason for this is that both the optics and the optic flow algorithms are still outperformed by their natural counterparts.

In our research we have drawn inspiration from all of the approaches above. In the next subsections, we report on three experiments and their results. As mentioned above, the DelFly is a passively stable MAV. Therefore, in our autonomy experiments we have limited ourselves to algorithms for controlling height and direction. The experiments we performed are: height control with an external camera (Subsection 5.2), height and direction control with a path-tracking algorithm (Subsection 5.3), and height control with an appearance-based algorithm (Subsection 5.4).

## 5.2 External camera algorithm

We performed our first autonomy experiment with the DelFly II with an external camera. The experiment had one main goal: to verify whether a good height estimate from external camera images would suffice for achieving height control. A height estimation algorithm for an external camera is easy to implement, reliable, and requires little computational effort. In addition, the external camera is directly connected to the computer performing the computational processing so that there is only a small delay in image transmission. For these reasons, the success of this experiment was a vital step towards more demanding algorithms that process the onboard images.

The experiment started with the pilot in full control of the DelFly. After trimming the throttle, he pushed the fire button to hand over throttle control to the height controller. The height controller first estimated the height of the DelFly with the following straightforward height estimation algorithm (see also Figure 18). The algorithm subtracted subsequent grayscale images from each other and applied a threshold to the result, in order to detect motion in the field of view. Then, the y-coordinates of all motion pixels were sorted to determine the median y-coordinate of the motion in the image. During the

experiment, only the DelFly moved in the field of view. The y-coordinate was scaled to the interval [-1,1], with 1 mapping to the top of the image and -1 to the bottom. Instead of attempting to calculate the exact height of the DelFly, the scaled y-coordinate was used as the error value for a regulator of the throttle. The regulator was a P-controller.
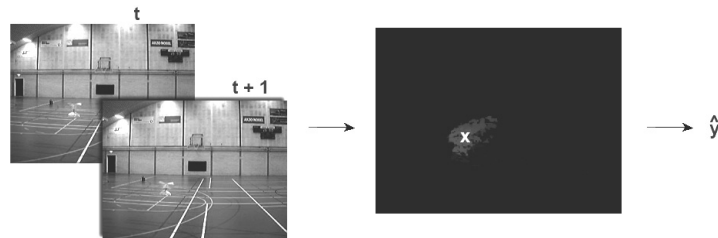


**Figure 18.** Illustration of the external camera algorithm. Two images captured at subsequent time steps are subtracted from each other, and thresholded. Then we estimate the median y-coordinate in the resulting binary motion mask.

Movies of two of the experiments can be seen online[19]. Figure 19 shows the median y-coordinate over time for the experiment of movie 'webcam2.avi'. Two peculiarities can be seen in the graph: (1) if no motion is present in the image, the output does not change (flat lines), and (2) if the DelFly leaves the image, the line will go flat and the DelFly will continue flying with the same throttle command. Therefore, if it leaves the view under the zero-level, it will usually return in view above the zero-level (abrupt changes in y-coordinate). However, for most of the run, the graph is smooth and the DelFly adjusts its throttle well in accordance to the y-estimates.
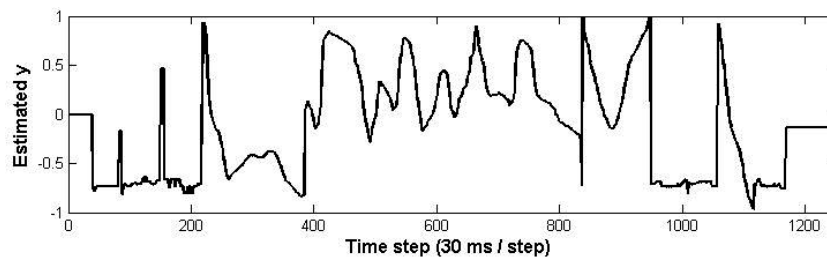


**Figure 19.** Median y-coordinate (y in [-1,1]) over time (~30ms per time step) for 'webcam2.avi'.

The above setup resulted in successful autonomous height control. During the flight, the pilot only had to steer the DelFly to keep it in the view of the webcam used as external camera. Importantly, a P-controller already sufficed for achieving height control.

## 5.3 Path-tracking algorithm

The second autonomy experiment had as main goal to test whether it was possible to achieve both height and direction control in a setting with onboard images. The bare minimum for full path control of a DelFly consists of 3 measurements. First, we need to estimate the height of the DelFly. The very low wing loading of DelFly makes it very well damped, so height measurements at more than about 5Hz are sufficient to stabilize its altitude within +/- 50cm. Second, the DelFly needs a measurement of the desired heading, in order to navigate to a point of interest. We cannot control the rudder only on the basis of this desired heading, since the DelFly is spiral unstable. So, third, we need to measure and control the turn rate. This is especially necessary for performing any sharp turns.

For the experiment, we designed an algorithm relying on the presence of a visible line on the ground, consisting of connected A4 papers (210 x 297 mm). The fixed size of the A4-papers was used for determining the height of the DelFly. The paper line itself was used as the path to follow. The reason for choosing a line was the image analysis simplicity and the fact that it easily applies to many buildings with long corridors, where seen from above the ground looks like a big line to follow in between the walls. In this experiment, the DelFly II had a dual camera setup with one camera pointing down and the other pointing forward. Two identical black and white cameras were used, since they have twenty

times better light sensitivity than color cameras. Below, we explain how we determined the height, desired heading, and turn rate from both cameras' images (see also Figure 20).
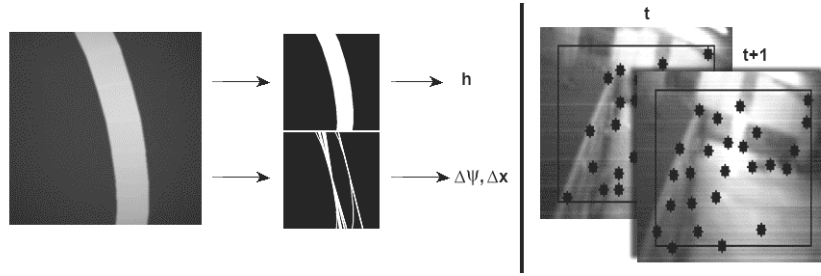


**Figure 20.** Illustration of image processing for the path-tracking algorithm. Left: the downward image is processed in two parallel ways to estimate the height (h), the desired relative heading ($\Delta\psi$), and the lateral offset ($\Delta x$). Right: Two subsequent forward images are processed to estimate the turn rate (r). See the text for more detail.

As mentioned, the fixed size of the A4 papers can be used for estimating the height. If the paper is in the centre of the view (no lateral offset), the height $h$ is related to the observed width of the a4 papers $p_{wA4}$ (in pixels) as:

$$ h = \frac{(w_{A4}/2)}{\tan\left(\frac{(p_{wA4}/2)(v/2)}{(p_{w\,\mathrm{Im}}/2)}\right)} \cos(\theta)\cos(\varphi) \tag{1} $$

where $w_{A4}$ is the width of an A4-sized paper in centimeters, $v$ is the field of view in degrees, $p_{w\,\mathrm{Im}}$ is the width of the image in pixels, and $\theta$ and $\varphi$ are the pitch and roll, respectively. Linearizing around zero pitch and zero roll simplifies this equation to:

$$ h = \frac{(w_{A4}p_{w\,\mathrm{Im}})}{p_{wA4}v} \tag{2} $$

Assuming a straight paper line running from the bottom to the top of the image, the surface of the line scales linearly with the width giving the final equation for height:

$$ h = \left(\frac{w_{A4}p_{h\,\mathrm{Im}}p_{w\,\mathrm{Im}}}{v}\right)/c \tag{3} $$

where $p_{h\mathrm{Im}}$ is the height of the image in pixels and c is the total number of paper pixels in view. Therefore, to estimate the height, we only need to measure the number of pixels in view belonging to the paper line. This was achieved by thresholding the image and counting the remaining pixels.

The desired heading was also obtained by processing the bottom image. We first performed Canny edge detection and then applied a coarse Hough line-detector (with 10 pixels and 5 degrees) in order to find the sides of the connected papers. Only detected lines pointing upwards within a 45 degree margin were used for estimation. Hence, horizontal lines were left out. Averaging the remaining lines gave the heading of the DelFly relative to the path $\Delta\psi$, and the lateral offset of the paper path $\Delta x$.

Finally, the turn rate $r$ was estimated with the help of subsequent images from the forward-pointing camera. Optic flow was computed on the images using the fast Lucas-Kanade algorithm[54] on a set of 40 corners in a 128 x 128 pixel resized image. Averaging the horizontal component of the optic flow results in a measure for the turn rate $r$.

Figure 21 is a diagram of the controller that has the four measurements ($h$, $\Delta\psi$, $\Delta x$, and $r$) as inputs, and the throttle and rudder deflection as control outputs. The track offset is converted to a desired heading angle using a P-gain. The difference in required heading en measured heading from the Hough detector are then converted to a desired turn rate using another P-gain. Finally, this desired turn rate minus the optic flow estimated turn rate are fed to the actuator using a final P-gain. The height is controlled with a straightforward P-regulator.
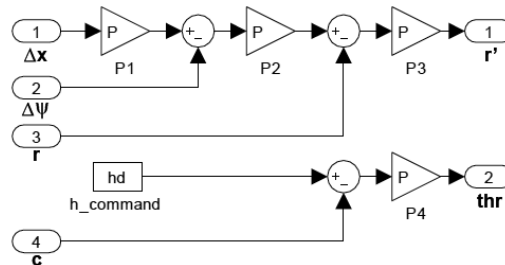


**Figure 21.** Controller used in the path-tracking experiment.

The main result of this experiment was that onboard images can be used for achieving autonomous height and direction control: the DelFly II was able to autonomously perform circles around two pillars and even performed an 8-figure in the EMAV 2008 indoor dynamics mission. Videos of these flights can be seen online[19]. Figure 22 shows the 3-D position of a simulated DelFly when performing an 8-figure in our simulator. It shows that the DelFly rises at the intersection of the 8-figure: since there is more paper in the image, the height is underestimated. Indeed, at the EMAV 2008 the DelFly also rose at the intersection[ii].

## 5.4 Appearance-based algorithm
The algorithm described above is limited to a room that has been specially prepared for the experiment: papers had to be put on the ground, indicating the DelFly's trajectory. When the conditions and assumptions of the algorithm are not satisfied (as in the case of the crossing of the 8-figure), the performance of the algorithm deteriorated. The state-of-the-art algorithms in autonomous indoor flight[46,47,48,53,52] all depend on specific properties of a room, be it the presence of texture or the visibility of parallel world lines. We would like to develop algorithms that are not dependent on such properties.
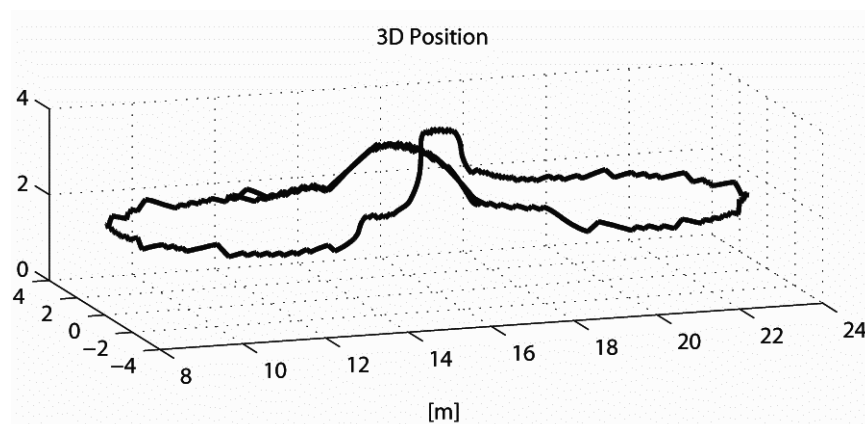


**Figure 22.** 3-D position of the DelFly during a flight in which it had to follow a 8-figure path. These data have been obtained in the simulator of 'SmartUAV'.

[ii]Instead of counting the number of pixels, we have also used the detected lines at the paper sides to estimate the height. However, this way of determining the height was more sensitive to noise in the images. In addition, it may have presented problems at the cross-point of the 8-figure as well, since more lines are detected in the image at that point.

As a first step, we discuss a height estimation algorithm that can be applied to any room with enough space for the DelFly to fly around. It is an appearance-based vision algorithm with the following important property: the computational effort of the algorithm can be reduced at the cost of a lower accuracy of the height estimates. The algorithm is based on the philosophy of *purposive vision*[55]: the state of the DelFly is explicitly estimated, but only to the extent necessary for autonomous flight. Hence, the algorithm may be situated in between the second and third approach described in Section 5.1. Below, we describe the algorithm and report on the results of our height control experiments with the DelFly II.

The height estimation algorithm is based on appearance differences between images taken at different heights, assuming little variance in the pitch of the MAV. Simply put: an image taken close to the ceiling is different from an image taken close to the floor. The algorithm is based on the work of Varma and Zisserman[56]. They showed that computationally intensive filtering methods (e.g., Gabor filters) were outperformed by the computationally efficient *texton* method on a texture classification task.
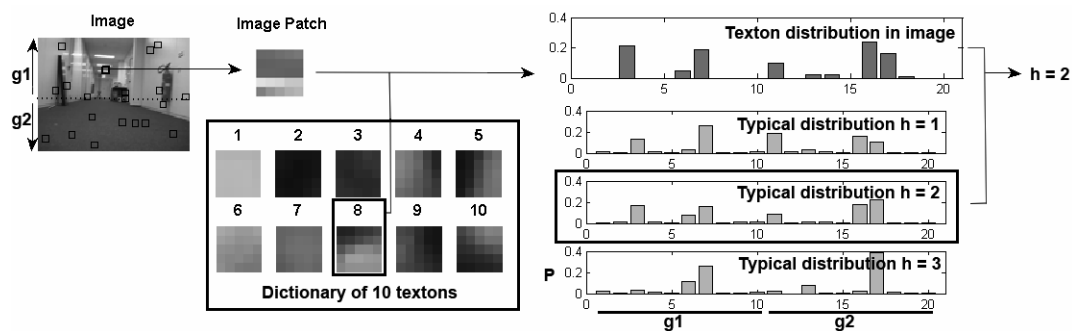


**Figure 23.** Illustration of the classification of an image as a height $h \in \{1,2,3\}$. First, $s$ patches are extracted from the image. Second, each patch is mapped to a texton in the dictionary consisting of $n$ textons. Depending on its place in the image (bottom or top half), one of the $2n$ bins in a histogram is incremented. Third, the normalized histogram is compared with the $H$ trained distributions. See the text for more details on the method.

We employ the texton method as follows. First, we make a training set of the forward camera images by walking around with the DelFly while holding it at $H$ distinct heights. The training starts by the formation of a *dictionary*, i.e., a collection of $n$ textons. To this end, we extracted many image patches of size 5 x 5 pixels (in 160 x 120 pixel images). These patches were clustered with a Kohonen network[57], resulting in $n$ cluster centroids – the textons. Then, we subdivide the training set into $H$ subsets of images taken at $H$ different heights. For each image in a subset, we extract $s$ image patches. Every image patch is mapped to the closest texton $w$. If the patch is extracted in the top half of the image, it is added to the $w^{th}$ bin of histogram $g1$, else it is added to $w^{th}$ bin of histogram $g2$. The image can now be represented as a histogram $g$, which is the concatenation of $g1$ and $g2$. By dividing $g$ by $s$, the number of samples, we get the maximum likelihood estimate of the probability distribution $p$ of the different textons occurring in the bottom and top half of the image. These distribution estimates can be used as feature vectors: in the experiments described below, we averaged the estimated distributions over all images of a subset to obtain a 'typical' distribution $p_h$ for a height $h$ ? $\{1,2,\dots,H\}$. After training, we classify an image as belonging to a certain height by estimating its distribution $p$ and then determining the closest distribution $p_h$ (Euclidian distance measure). This straightforward nearest neighbor method resulted in a height classification error of ~22% on a test set of images which was not used during the training process. Figure 23 illustrates the process.

Figure 24 shows the classification error (represented as the ratio of misclassified images / total images in the test set) for an image set in which H = 3, $n \varepsilon \{2, 5, 10, 20, 30\}$, and $s \varepsilon \{10, 50, 100, 200, 300\}$. The mean error is illustrated by the gray surface, the standard deviation by the transparent white surfaces. Increasing the number of samples improves the performance, but the effect is largest for $s <$ 100. The number of words seems to have an optimum around 10: a smaller number results in a dictionary which is not expressive enough, while a larger number results in overfitting (cf. [58]).
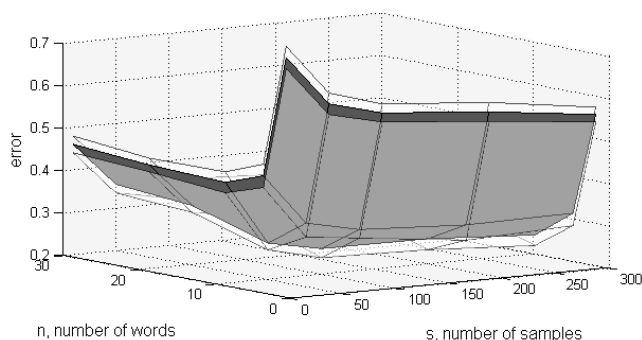
**Figure 24.** Classification error for $n \, \varepsilon \, \{2, 5, 10, 20, 30\}$, and $s \, \varepsilon \, \{10, 50, 100, 200, 300\}$. The mean error is shown with a gray surface, the standard deviation with transparent white surfaces.

For the height control, we used $n = 10$ words, and $H = 5$. The height $h$ was linearly scaled to $[-1,1]$, with $h = 1$ mapped to -1 and $h = 5$ mapped to 1. $h$ was subsequently processed by a Butterworth filter of order 2 and with a cutoff of 0.305. The resulting value was used as the error value in a P-regulator.

Before executing the height controller, we determined the number of samples that would be used. The left part of Figure 25 shows the relation between the execution frequency of the thread running the height estimation algorithm in relation to the number of samples. These measurements were done on a Dual Core Intel processor at 2.27GHz. Please note that at the time of measurement, the laptop was also running the video capture software, the controller, various output windows, and the communication with an RC remote. We decided to use $s = 100$ samples, to ensure both a reasonable speed and accuracy.
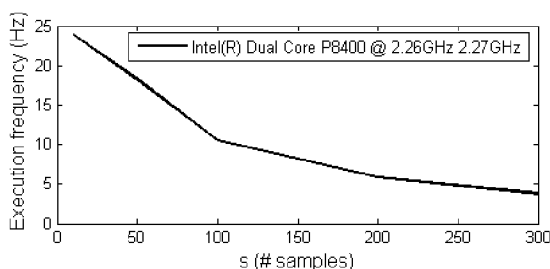


**Figure 25.** *Left*: Execution frequency vs. number of samples s. *Right*: Experiment room.

We tested the height control in an office room that had no other preparation than switching on the lights and pushing the furniture aside (see the right part of Figure 25). After training in the room, the DelFly II successfully maintained a sane height during the experiment; it neither touched the floor nor got close to the ceiling. Since we filmed the DelFly with two external cameras, we were able to estimate its three-dimensional position during the flight. Figure 26 shows the three-dimensional position of the DelFly (left) and the estimated height during the experiment (right). The experiment ended, because the battery ran out. We hope to perform experiments with new DelFlys soon, in order to test whether it is necessary to adapt the controller over the battery's life.

The results presented above are obtained in the room that was also used for training. Of course, for any autonomy of interest, the height control should generalize to other rooms than the training room. We did not test this aspect yet, although it was encouraging that the learned dictionary and distributions were effective at different times during the day. This means that the method is not too sensitive to lighting conditions. A straightforward option to achieve generalization to different rooms is to constitute a large training set of images taken in many different office rooms. Another option is to include other visual features than appearance alone, such as optic flow. In any case, we have to solve this matter in order for the algorithm to be useful for achieving full autonomous flight.
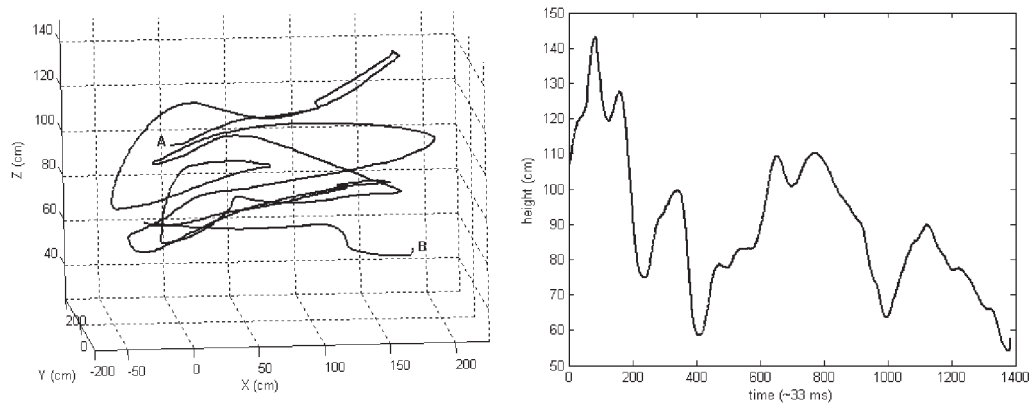
**Figure 26.** Left: Three-dimensional position during one of the height control experiments. Right: Corresponding height of the DelFly over time.
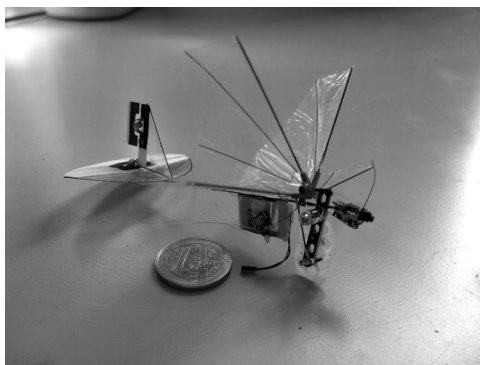
## 6. DELFLY MICRO & BEYOND
### 6.1 DelFly Micro

The research on the DelFly I and DelFly II have led to the successful development of the DelFly Micro: a 3.07 gram weighing ornithopter with a wing span of 10 cm (Figure 27). There are other micro-sized flying ornithopters[59,60]. The one described in [59] was inspired on the DelFly Micro and is currently the smallest flying ornithopter: it has a 6 cm wing span and weighs 1.47g. However, the DelFly Micro is still the smallest flying ornithopter with a camera and transmitter onboard.

At the small scale of the DelFly Micro it is absolutely necessary to get the maximum out all of its components. The design of the DelFly Micro relies heavily on the advances made on the DelFly I and II concerning the crank mechanism, tail, wing shape, radio control, video system, and insight into the aerodynamics. In addition, advances made on other platforms have been taken into account. For example, the 10cm ornithopter in [60] had an additional clap and fling at the middle of the flap. Without all the aforementioned advances, the DelFly Micro would most probably not have been able to gain altitude during its flight. Therefore, we regard the successful flights of the DelFly Micro as our strongest argument for a top-down approach. Movies of these flights can be seen online[19].

Moreover, having the DelFly I and II allowed us to put in place all necessary elements for autonomy experiments: ranging from a ground station to the development of vision and control algorithms. Since our research on autonomy has focused on a platform with as only sensor a camera, the algorithms that we currently test out on the DelFly II can equally be applied to the DelFly Micro. The only hurdle to be taken in this respect is the flight duration and performance of the DelFly Micro. The current version of the Micro cannot generate sufficient thrust for hovering, due to overheating of its brushed motors. A careful reader will notice that similar problems have been experienced with the DelFly I, and that a probable solution lies in the adoption of an adapted brushless motor. Our main challenge at the moment is to achieve hovering flight of the DelFly Micro.



| Total mass | 3.07 gr |
|---|---|
| Battery | 1.00 gr |
| Camera and transmitter | 0.40 gr |
| Motor | 0.45 gr |
| Receiver | 0.20 gr |
| Actuators | 0.50 gr |
| Rest | 0.52 gr |

**Figure 27.** Left: DelFly Micro next to a Euro coin. Right: Mass of the parts.

## 6.2 Challenges Ahead

We have stated in the introduction that our long-term goal is to arrive at fly-sized MAVs that can fly autonomously in complex environments. We now discuss the essence of the related challenges and how we plan to approach them.

First and foremost, the main challenge for achieving a small span *size* of the ornithopter lies in reducing the weights of all other components. Namely, it is easier to reduce the size of an ornithopter than to reduce its weight. Reducing an ornithopter's wing size by two roughly comes down to a multiplication of the wing loading by four, if the weight remains constant. As a consequence, the weight of all components together should be reduced by a factor four – which is generally not possible in the same time span. Any smaller factor results in a higher wing loading for the new, smaller model. In turn, this signifies that not only should the new components be smaller than the old ones, they should also perform better. Better performance is hard to obtain, since at smaller sizes the mechanical, energy, and aerodynamic efficiencies degrade. For example, a smaller drive mechanism has relatively more friction than a larger one. This size dilemma is already noticeable at the scale of the DelFly Micro, and is the reason that we feel that some parts of the DelFly should undergo a thorough change in order to enable a DelFly Nano of ~5 cm. One of the candidates for such a change is the drive mechanism. The crank-mechanism actively operates the wing during all phases of the flap. Instead, natural systems and artificial systems of the bottom-up approach[2,14] exploit the *resonance* of the system. Designing a resonant drive mechanism may be a necessary step towards smaller sizes.

Second, at smaller scales, the ***autonomy*** of the ornithopter becomes increasingly important. At a smaller size scale the movements of the ornithopter occur at a smaller time scale as well. A reason for this is the increasingly large mass in relation to the aerodynamic dampening. The smaller size and time scales give more difficulties to a human pilot. The attitude of the ornithopter is more difficult to discern visually, especially at larger distances. In addition, the movements are harder to predict and the pilot needs to react quicker. In short, at very small sizes the passive stability properties of the larger DelFlys may degrade, requiring active stability augmentation. To accommodate this on the long term, we do not only focus on the size of ornithopters but also on reducing the weight of the existing platforms. Weight reduction allows the addition of sensors and onboard processing. Currently, only a few ultra-light MAVs have experimented with onboard processing. For example, the work in [50] concerned a 10-gram micro flyer that processed the inputs from a linear pixel-array onboard. It achieved autonomous flight in a textured experiment room. In order to process two-dimensional images, advances have to be made in the above-mentioned weight reduction and in the design of computationally efficient autonomy algorithms. The algorithm explained in Subsection 5.4 seems a promising candidate for such an onboard processing scheme, if it can generalize over many indoor situations.

Both challenges play a role in the possible application of ornithopters to real-world problems. An illustration of this was given by the events that occurred at the Technical University of Delft. In May 2008, a fire ravaged the building of the faculty of architecture. After the fire was extinguished, the building was in danger of collapsing – preventing the inspection of the inside of the building. Therefore, it was unclear whether some of the precious furniture and book collections inside the building survived the fire. Our group offered to make images of the building with a DelFly II. We were able to capture images of higher floors by looking through the windows. The left part of Figure 28 shows an image of the faculty building. We also attempted to enter the building with the DelFly. However, the openings in the shattered windows were too small and there was too much turbulence around the building. As a consequence, it was too risky for a human pilot to steer the DelFly into the building. Before the DelFly landed, it received acknowledgment by nature: it was attacked by a crow, shown in the right part of Figure 28. We hope that our research on smaller, more autonomous ornithopters might contribute to similar tasks in the future – both the exploration of dangerous places and the filming of nature.
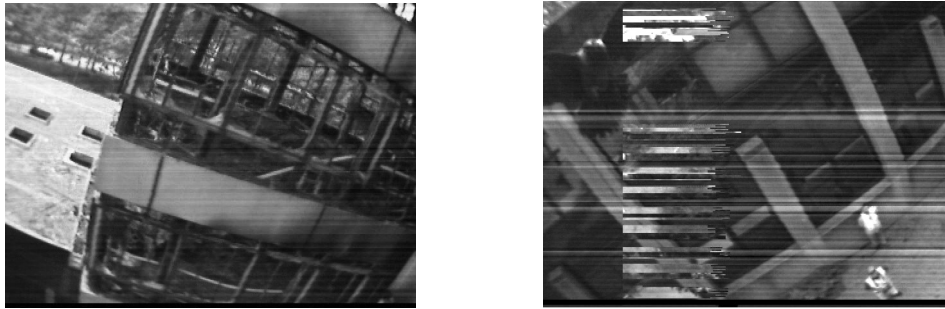
**Figure 28.** Left: Image of the faculty building of architecture. Right: Crow attacking the DelFly II (top left in the image).

## REFERENCES

1    Pornsin-sirirak, T. N.,  Lee, S. W., Nassef, H., Grasmeyer, J., Tai, Y. C., Ho, C. M., and Keennon, M. (2000) "MEMS wing technology for a battery-powered ornithopter." *13th IEEE International Conference on Micro Electro Mechanical Systems, (MEMS 2000)* , Miyazaki, Japan, Piscataway, NJ, pp. 799-804, 2000.

2    Wood, R.J. "The first takeoff of a biologically-inspired at-scale robotic insect", *IEEE Tranactions on Robotics*, Vol. 24, No. 2, pp. 341-347, April, 2008.

3    Michelson, R.C. "Test and Evaluation for Fully Autonomous Micro Air Vehicles", *The ITEA Journal*, Volume 29, Number 4, pp. 367 – 374, December, 2008

4    Michelson, R.C. and Naqvi, M.A, "Beyond Biologically-Inspired Insect Flight," *von Karman Institute for Fluid Dynamics RTO/AVT Lecture Series on Low Reynolds Number Aerodynamics on Aircraft Including Applications in Emerging UAV Technology*, Brussels Belgium, 24-28 November, 2003

5    van Breugel, F., Regan W., and Lipson, H. "Passively Stable Flapping Hovering Micro Air Vehicle." *International Symposium on Flying Insects and Robotics*, pp. 15-16, August, 2007.

6    Boria, F.J., Bachmann, R.J., Ifju, P.G., Quinn, R.D., Vaidyanathan, R., Perry, C., and Wagener, J. (2005) "A Sensor Platform Capable of Aerial and Terrestrial Locomotion", *Intelligent Robots and Systems (IROS)*, Alberta, Canada, August. 2-6, 2005.

7    Mueller, T. J. and DeLaurier J.D., "Aerodynamics of small vehicles", *Annual Review of Fluid Mechanics*, Volume 35, pp. 89–111, 2003.

8    Keennon M.T. and Grasmeyer J.M., "Development of the Black Widow and Microbat MAVs and a Vision of the Future of MAV Design", *AIAA International Air and Space Symposium and Exposition: The Next 100 Years*, Dayton, Ohio, July 14-17, 2003

9    Malladi B., Krashanitsa R., Silin D., and Shkarayev S., "Dynamic Model and System Identification Procedure for Autonomous Ornithopter", *Online presentation*, The University of Arizona, Tucson, AZ, USA

10   Ansari, S. A., ?bikowski, R., and Knowles, K. "Aerodynamic modelling of insect-like flapping flight for micro air vehicles", *Progress in Aerospace Sciences*, Volume 42, Issue 2, pp. 129-172, 2006.

11    Malolan, V. , Dineshkumar, M., and Baskar, V., "Design and development of flapping wing micro air vehicle", *42nd AIAA Aerospace Sciences Meeting and Exhibit*, 5 - 8 January, Reno, Nevada, 2004.

12    Ellington, C.P., Berg, C. van den, Willmott, A.P., and Thomas, A.L.R. "Leading-edge vortices in insect flight" *Nature* Vol. 384, Issue 19/26, pp. 626-630, 1996.

13    Dickinson, M.H., Lehmann F.-O., and Sane, S.P., "Wing Rotation and the Aerodynamic Basis of Insect Flight", *Science*, Vol. 284. no. 5422, pp. 1954 – 1960, 1999.

14    Steltz, E., Avadhanula, S., and Fearing, R.S., "High Lift Force with 275 Hz Wing Beat in MFI", *IEEE International Conference on Intelligent Robots and Systems*, San Diego, October, 2007.

15    Steltz, E. and Fearing, R.S., "Dynamometer Power Output Measurements of Piezoelectric Actuators", *IEEE International Conference on Intelligent Robots and Systems*, San Diego, October, 2007.

16    Brooks, R. A., "Elephants don't play chess.", *Robotics and Autonomous Systems*, Volume 6, Numbers 1–2, pp. 3–15, 1990.

17    Pfeifer, R. and Scheier, C. "Understanding Intelligence." *MIT Press*, Cambridge, MA, 1999.

18    Nolfi, S. and Floreano, D. "Evolutionary Robotics: The Biology, Intelligence, and Technology of Self-Organizing Machines.", *MIT Press / Bradford Books*, Cambridge, MA, 2000.

19    http://www.delfly.nl/

20    Jongerius S.R., Straathof M.H., van der Veen G.J., Roos W.V.J., Moelans P., Lagarde R.C.A., Kacgor A.N.A., Heynze C.J.G., Ashok A., de Clercq K.M.E., and van Ginneken D.A.J., "Design of a flapping wing vision-based Micro-UAV", *Design synthesis exercise*, *Faculty of Aerospace Engineering, TU Delft*, 2005.

21    http://www.flyabird.com/ff.html

22    Bradshaw, N.L., and Lentink, D. "Aerodynamic and structural dynamic identification of a flapping wing micro air vehicle", *American Institute of Aeronautics and Astronautics, 26th AIAA Applied Aerodynamics Conference*, 2008.

23    Ellington, C.P., "Unsteady aerodynamics of insect flight." *Biological Fluid Dynamics*. ed. C.P. Ellington and T.J. Pedley. Symp. Soc. exp. Biol. Volume 49, pp. 109-129, 1995.

24    Anderson, J.D. "Fundamentals of aerodynamics", *Mc Graw-Hill*, 2001.

25    Ellington,C.P., "The aerodynamics of hovering insect flight. IV. Aerodynamic mechanisms" *Phil. Trans. R. Soc. Lond.* B 305, pp. 79-113, 1984.

26    Willmot, P.W., Elington, C.P., Thomas, A.L.R., "Flow visualization and unsteady aerodynamics in the flight of the hawkmoth, Manduca Sexta" *Phil. Trans.*, 1997.

27    Van den Berg, C., Ellington, C.P., "The three-dimensional leading-edge vortex of a 'hovering' model hawkmoth" *Phil. Trans. R. Soc. Lond.* B 352, pp. 329-340, 1997.

28    Maxworthy,T., "Experiments on the Weis-Fogh mechanism of lift generation by insects in hovering flight. Part 1. Dynamics of the 'fling'" *Journal of Fluid Mechanics*, vol. 93, part 1, pp.47-63, 1979.

29    Lehmann, F.O., Sane, P.S., Dickinson, M., "The aerodynamic effects of wing-wing interaction in flapping insect wings" *Journal of Experimental Biology*, Volume 208, pp. 3075-3092, 2005.

30    Poelma, C.; Dickson, W.B.; Dickinson, M.H. "Time-resolved reconstruction of the full velocity field around a dynamically-scaled flapping wing" *Experiments in Fluids* Volume 41, pp. 213-225, 2006.

31    De Clercq, K.M., de Kat, R., Remes, B., "Flow visualization and force measurements on a hovering flapping-wing MAV 'DelFly II'", *American Institute of Aeronautics and Astronautics, 39th AIAA Applied Aerodynamics Conference* (accepted)

32    Ellington, C.P., "The aerodynamics of hovering insect flight. III. Kinematics" *Phil. Trans. R. Soc. Lond.* B 305, pp. 79-113, 1984.

33    Lehmann, F.O., Pick, S., "The aerodynamic benefit of wing-wing interaction depends on stroke trajectory in flapping insect wings", *Journal of Experimental Biology*, Volume 210, pp. 1362-1377, 2007.

34    www.didel.com

35    www.microbrushless.com

36    Ma, C.C., Wang, R., Sun, Q.P., Zohar, Y., Wong, M., "Frequency response of TiNi shape memory alloy thin film micro-actuators", *13th Annual International Conference on Micro Electro Mechanical Systems (MEMS 2000)*, pp. 370-374, 2000.

37    www.bsdmicrorc.com

38    Leven, S., Zufferey, J.-C., and Floreano, D., "A Simple and Robust Fixed-Wing Platform for Outdoor Flying Robot Experiments." *International Symposium on Flying Insects and Robots*, Monte Verità, Locarno, Switzerland, August 12-17, pp. 69-70, 2007.

39    Kannan, S.K., and Johnson, E.N., "Adaptive Trajectory based Control for Autonomous Helicopters.", *21st Digital Avionics Systems Conference*, Irvine, CA, October, 2002.

40    Johnson, E.N., and Kannan, S.K., "Adaptive Flight Control for an Autonomous Unmanned Helicopter.", *AIAA Guidance, Navigation, and Control Conference and Exhibit*, Monterey, California, August, 2002

41    Grzywna, J.W., Plew, J., Nechyba, M.C., and Ifju, P.G., "Enabling Autonomous MAV Flight", *16th Florida Conference on Recent Advances in Robotics*, 2003.

42    Elfes, A., Montgomery, J.F., Hall, J.L., Joshi, S.S., Payne, J., and Bergh, C.F., "Autonomous flight control for a Titan exploration aerobot." *8th International Symposium on Artificial Intelligence, Robotics and Automation in Space (i-SAIRAS 2005)*, ed. B. Battrick. ESA SP-603. European Space Agency, p.91.1, 2005.

43    Thrun, S., Burgard,W., and Fox, D. "Probabilistic Robotics.", *MIT Press*, Cambridge, MA, 2005.

44    Mak, L.C., Whitty, M., Furukawa, T., "A localisation system for an indoor rotary-wing MAV using blade mounted LEDs.", *Sensor Review*, Volume 28, Number 2, pp. 125-131, 2008.

45    Rudol, P., Wzorek, M., Conte, G., and Doherty, P., "Micro Unmanned Aerial Vehicle Visual Servoing for Cooperative Indoor Exploration.", *Proceedings of the 2008 IEEE Aerospace Conference*, 2008.

46    Kemp, C., "Visual Control of a Quad-Rotor Helicopter.", *Ph.D. Thesis, Churchill College, University of Cambridge*, 2006.

47    Elik, K.C., Chung, S.-J., and Somani, A., "Mono-Vision Corner SLAM for Indoor Navigation.", *IEEE International Conference on Electro/Information Technology 2008*, pp. 343-348, 2008.

48    Ahrens S., "Vision-Based Guidance and Control of a Hovering Vehicle in Unknown Environments", *M.Sc. Thesis, MIT* SM, June, 2008.

49    Johnson N., "Vision-assisted control of a hovering air vehicle in an indoor setting", *M.Sc. thesis, Brigham Young University*, 2008.

50    Zufferey, J.-C., Klaptocz, A., Beyeler, A., Nicoud, J.-D., and Floreano, D., "A 10-gram Microflyer for Vision-based Indoor Navigation", *Proceedings of the 2006 IEEE/RSJ International Conference on Intelligent Robots and Systems* October 9 - 15, Beijing, China, 2006.

51    Iida, F., "Goal-directed navigation of an autonomous flying robot using biologically inspired cheap vision.", *Proceedings of the 32nd ISR (International Symposium on Robotics)*, 2001.

52    Humbert, J.S., and Frye, M.A., "Extracting behaviorally relevant retinal image motion cues via wide-field integration." *American Control Conference*, number 14–16, pp. 6, 2006

53    Beyeler, A., Zufferey, J-C., and Floreano, D. "3d vision-based navigation for indoor microflyers.", *IEEE International Conference on Robotics and Automation 2007*, Roma, Italy, pp. 1336–1341, 2007

54    Open CV: http://sourceforge.net/projects/opencvlibrary/

55    Aloimonos, J., "Purposive and qualitative active vision.", *10th International Conference on Pattern Recognition*, volume 1, pp. 346–360, Atlantic City, NJ, 1990.

56    Varma M., and Zisserman. A., "Texture classification: are filter banks necessary?" *IEEE Computer Society Conference on Computer Vision and Pattern Recognition (CVPR 2003)*, Madison, WI, volume 2, pp. 691–698. IEEE Computer Society, 2003.

57    Kohonen, T., "Self-Organizing Maps", 3rd edition, *Springer Series in Information Sciences*, Vol. 30. Springer, 2001.

58  Bishop, C.M., "Pattern recognition and machine learning." *Springer Science and Business Media*, LLC, New York, NY, 2006.

59  Takahashi, Y. *Blog*: http://blog.goo.ne.jp/flappingwing/e/722e1073f96aaccd8892ea63f8240ded, *Movie*: http://www.youtube.com/watch?v=zo-69d5AF-o

60  Satoshi, S., and Yoshiyuki, K. "Development of a Flapping Micro Air Vehicle With Hovering Ability.", *Nihon Kikai Gakkai Ryutai Kogaku Bumon Koenkai Koen Ronbunshu*